Quantum Simulation of Light-Matter Interaction Models

Diogo Ramos
Faculdade de Ciências (FCUP), Universidade do Porto, Portugal
(Dated: December 22, 2025)

I. Introduction

The simulation of quantum systems is one of the most promising applications of quantum computing, offering the potential to investigate physical phenomena that are intractable for classical computers in the future [1, 2]. Among the most significant classes of such systems are those involving the interaction between matter and quantized bosonic fields, which are ubiquitous in physics. These interactions are fundamental to a wide range of disciplines, from quantum optics and condensed matter physics to quantum chemistry.

A central challenge in simulating these systems on qubit-based hardware is the infinite-dimensional nature of the bosonic Hilbert space. Unlike spin systems, which map naturally onto qubits, bosonic modes (such as harmonic oscillators or cavity modes) require a truncation of their state space to be represented on finite-dimensional quantum registers [3]. This truncation must be handled with care since if the cutoff is too low, the simulation may fail to capture essential dynamics and if too high, it incurs unnecessary resource overheads in terms of qubit count and gate complexity.

State-of-the-art approaches to this problem involve systematic truncation procedures combined with rigorous error analysis. Recent advances have focused on developing bounds that control two specific types of errors: the initial state truncation error and the dynamical leakage error [4, 5]. The tail-control guarantee ensures that the truncated initial state faithfully represents the physical state [3], while dynamical leakage bounds account for the spreading of the wavefunction into higher photon-number states during time evolution [5].

To implement these simulations practically, the truncated bosonic operators must be mapped to qubit operators. Several encoding schemes have been proposed, each offering different trade-offs [6]. Unary encodings preserve locality but are resource-intensive, requiring $\mathcal{O}(N)$ qubits for a truncation dimension N. Binary encodings, utilizing $N_q = \lceil \log_2 N \rceil$ qubits, offer logarithmic resource efficiency but often result in non-local operator strings. More recently [7], symmetry-aware encodings have emerged as a powerful alternative for systems possessing conservation laws which by restricting dynamics to invariant subspaces, can eliminate leakage errors and significantly reduce qubit overhead.

This work explores these simulation strategies within the context of light-matter interaction models, specifically the Jaynes-Cummings and Quantum Rabi models. We leverage rigorous error bounds to determine optimal truncation cutoffs, demonstrating how these techniques can be applied to simulate phenomena such as collapse and revival of Rabi oscillations and vacuum instability in the ultrastrong coupling regime.

II. Bosonic systems and truncation

Bosonic degrees of freedom, such as harmonic oscillators, cavity modes and vibrational modes, are central to quantum optics. However, since each bosonic mode is endowed with an infinite-dimensional Hilbert space, in the context of qubit-based quantum simulation this can be problematic. To circumvent this, one needs a systematic finite-dimensional truncation procedure accompanied with pragmatic error bounds that can then be used to design efficient and precise simulation schemes.

The canonical bosonic mode is described by the annihilation and creation operators, denoted a and $a^\dagger$ respectively, which satisfy the commutation relations

$$[a_i, a_j^\dagger] = \delta_{ij}, \quad [a_i, a_j] = 0, \quad [a_i^\dagger, a_j^\dagger] = 0.$$

By defining the number operator as $n_i = a_i^\dagger a_i$, one can construct the Fock basis $\{|n\rangle\}_{n=0}^{\infty}$ where $|n\rangle$ denotes the eigenstate of n with eigenvalue n.

In order to represent this infinite-dimensional space on a finite qubit register we are forced to truncate the Fock basis to the subspace

$$\mathcal{H}_N \;=\; \mathrm{span}\{|0\rangle, |1\rangle, \ldots, |N-1\rangle\}.$$

This leads naturally to the definition of the truncated annihilation and creation operators by their action on this new basis:

$$a^{(N)} = \sum_{n=0}^{N-2} \sqrt{n+1}\, |n\rangle \langle n+1|, \tag{1}$$

$$a^{(N)\dagger} = \sum_{n=0}^{N-2} \sqrt{n+1}\, |n+1\rangle \langle n|, \tag{2}$$

$$n^{(N)} = a^{(N)\dagger} a^{(N)} \;=\; \sum_{n=0}^{N-1} n\, |n\rangle \langle n|. \tag{3}$$

With the Fock ordering $\{|0\rangle, |1\rangle, \ldots, |N-1\rangle\}$ these operators can be represented as the following $N \times N$

matrices

$$a^{(N)} = \begin{pmatrix} 0 & \sqrt{1} & 0 & \cdots & 0 \\ 0 & 0 & \sqrt{2} & \cdots & 0 \\ \vdots & & \ddots & \ddots & \vdots \\ 0 & 0 & \cdots & 0 & \sqrt{N-1} \\ 0 & 0 & \cdots & 0 & 0 \end{pmatrix}. \tag{4}$$

$$a^{(N)\dagger} = \begin{pmatrix} 0 & 0 & 0 & \cdots & 0 \\ \sqrt{1} & 0 & 0 & \cdots & 0 \\ 0 & \sqrt{2} & 0 & \cdots & 0 \\ \vdots & & \ddots & \ddots & \vdots \\ 0 & 0 & \cdots & \sqrt{N-1} & 0 \end{pmatrix}. \tag{5}$$

$$n^{(N)} = \mathrm{diag}(0, 1, 2, \ldots, N-1). \tag{6}$$

As long as the truncation dimension N is sufficiently large, these explicit finite matrices and the associated finite space can be embedded into qubit registers and subsequently be used to simulate bosonic dynamics, such as light matter interactions.

The approximation error induced in this process is entirely dependent on the system being simulated, however general bounds can often be applied in resource estimates.

Two complementary certification strategies that are commonly employed in rigorous and practical analyses of finite-dimensional truncations for bosonic modes are (i) control of the initial population tail and its direct effect on observables, and (ii) control of dynamical leakage during the evolution via number-raising bounds.

Theorem II.1 (Tail-control guarantee)**.** *Let* $\Pi_N = \sum_{n=0}^{N-1} |n\rangle\langle n|$ *denote the orthogonal projector onto the truncated Fock subspace of dimension* N *(*$\mathcal{H}_N = \mathrm{Ran}\,\Pi_N$*), and let* ρ *be the true initial state of the bosonic mode. Define the tail weight*

$$p_{\mathrm{tail}}(N) \coloneqq 1 - \mathrm{Tr}(\Pi_N \rho).$$

For any bounded observable O *with operator norm* $\|O\| \leq 1$*, replacing* ρ *by the truncated state* $\Pi_N \rho \Pi_N$ *changes expectation values by at most a quantity proportional to the tail,*

$$\left|\,\mathrm{Tr}[O(\rho - \Pi_N \rho \Pi_N)]\right| \;\leq\; 2\, p_{\mathrm{tail}}(N).$$

Consequently, if $p_{\mathrm{tail}}(N) \leq \varepsilon/2$ then all unit-norm-bounded observables incur error bounded by ε. Practical estimation or direct numerical sampling of $p_{\mathrm{tail}}(N)$ is sufficient to certify that the truncation is initially benign [4, 8].

While the tail-control guarantee addresses the truncation of the initial state, ensuring the accuracy of the time evolution requires a more rigorous analysis of how the Hamiltonian couples different Fock states. To bound the dynamical leakage, we adopt the framework of Tong *et al.* [5], referring to Refs. [5, 9] for a more detailed exposition and proofs.

Define $\Pi_\lambda = |\lambda\rangle\langle\lambda|$ as the projector onto the specific number state $|\lambda\rangle$, and $\Pi_{[0,\Lambda]} = \sum_{\lambda=0}^{\Lambda} \Pi_\lambda$ as the projector onto the subspace containing states with up to Λ particles. Now consider a Hamiltonian H which admits a decomposition into a number-conserving term H_r and a number-changing interaction term H_w

$$H = H_w + H_r, \tag{7}$$

subject to the following three constraints characterized by a coupling parameter $\chi > 0$ and a scaling exponent $0 \leq r < 1$:

1. **Bandwidth Constraint:** The interaction H_w changes the boson number by at most one:
$$\Pi_\lambda H_w \Pi_{\lambda'} = 0 \quad (\text{if } |\lambda - \lambda'| > 1). \tag{8}$$
2. **Norm Growth Constraint:** The norm of the interaction term restricted to a finite box grows polynomially with the cutoff:
$$\|H_w \Pi_{[0,\Lambda]}\| \leq \chi(\Lambda + 1)^r. \tag{9}$$
3. **Diagonal Constraint:** The term H_r is diagonal in the number basis (preserves boson number):
$$[H_r, \Pi_\lambda] = 0. \tag{10}$$

Given that these conditions are satisfied we can infer the bound for the error incurred by replacing the ideal evolution e^{-itH} with the evolution generated by the truncated Hamiltonian $\tilde{H} \coloneqq \Pi_{[0,\tilde{\Lambda}]} H \Pi_{[0,\tilde{\Lambda}]}$.

Theorem II.2 (Bosonic Hamiltonian Truncation)**.** *Given a bosonic Hamiltonian* $H = H_w + H_r$ *satisfying the conditions above with parameter* $\chi > 0$*, for any time* $t > 0$*, error tolerance* $\epsilon > 0$*, and initial maximum particle number* $\Lambda_0 > 0$*, there exists a truncation cutoff* $\tilde{\Lambda}$ *such that the evolution error on the initial subspace is bounded by* ϵ*:*

$$\|e^{-itH}\Pi_{[0,\Lambda_0]} - e^{-it\tilde{H}}\Pi_{[0,\Lambda_0]}\| \leq \epsilon. \tag{11}$$

The required truncation cutoff $\tilde{\Lambda}$ *scales asymptotically as:*

$$\sqrt{\tilde{\Lambda}} = \sqrt{\Lambda_0} + \mathcal{O}\left(\chi t \log\left(\frac{\Lambda_0 \chi t}{\epsilon}\right)\right). \tag{12}$$

III. Qubit Mappings

After picking a suitable cutoff for the Hilbert Space, the sparse matrix representations of the creation and annihilation operators given by Eqs. (4)–(6) must be mapped to feasible operations on a qubit register. Several mappings have been proposed in the literature, each with its own advantages and disadvantages in terms of qubit efficiency, operator locality, and gate complexity. In this section we discuss three widely-used encoding archetypes: unary encoding, binary encoding, and symetry-aware encoding.

A. Unary Encoding

The unary encoding maps each Fock state $|n\rangle$ (where $0 \leq n \leq N-1$) to a state of N qubits, where exactly one qubit is in the excited state $|1\rangle$ and all others are in $|0\rangle$. Specifically, the state $|n\rangle$ is mapped to a tensor product where the n-th qubit is $|1\rangle$:

$$|n\rangle \mapsto |0\rangle_0 \otimes \cdots \otimes |0\rangle_{n-1} \otimes |1\rangle_n \otimes |0\rangle_{n+1} \otimes \cdots \otimes |0\rangle_{N-1}. \quad (13)$$

In this representation, the creation operator $a^{(N)\dagger}$, which transitions the system from $|n\rangle$ to $|n+1\rangle$, can be expressed using the qubit ladder operators $\sigma_+ = |0\rangle\langle 1|$ and $\sigma_- = |1\rangle\langle 0|$ as:

$$a^{(N)\dagger} = \sum_{n=0}^{N-2} \sqrt{n+1} \left(\sigma_+^{(n)} \otimes \sigma_-^{(n+1)} \right). \quad (14)$$

Analogously, the annihilation operator $a^{(N)}$ is given by:

$$a^{(N)} = \sum_{n=0}^{N-2} \sqrt{n+1} \left(\sigma_-^{(n-1)} \otimes \sigma_+^{(n)} \right), \quad (15)$$

where the operators act non-trivially only on the n-th and $(n \pm 1)$-th qubits:

$$\sigma_\pm^{(n)} = I^{\otimes n} \otimes \sigma_\pm \otimes I^{\otimes (N-n-1)}. \quad (16)$$

These ladder operators can be further decomposed into Pauli operators, mapping directly to qubit gates:

$$\sigma_+ = \frac{X + iY}{2}, \quad \sigma_- = \frac{X - iY}{2}. \quad (17)$$

While this encoding offers a simple local (nearest-neighbor) structure for hopping terms, it is qubit-inefficient, requiring $\mathcal{O}(N)$ qubits to represent N states.

B. Binary Encoding

To improve qubit efficiency, the binary encoding maps the index n of the Fock state $|n\rangle$ to its binary representation using $N_q = \lceil \log_2 N \rceil$ qubits. The mapping is defined as:

$$|n\rangle \mapsto \left| b_{N_q-1} \cdots b_0 \right\rangle, \quad \text{where } n = \sum_{k=0}^{N_q-1} b_k 2^k. \quad (18)$$

For instance, we can write

$$\begin{aligned} |0\rangle &\mapsto \left|0_{N_q-1}\right\rangle \otimes \cdots \otimes |0_1\rangle \otimes |0_0\rangle, \\ |1\rangle &\mapsto \left|0_{N_q-1}\right\rangle \otimes \cdots \otimes |0_1\rangle \otimes |1_0\rangle, \\ |2\rangle &\mapsto \left|0_{N_q-1}\right\rangle \otimes \cdots \otimes |1_1\rangle \otimes |0_0\rangle, \\ &\vdots \\ \left|2^{N_q}-1\right\rangle &\mapsto \left|1_{N_q-1}\right\rangle \otimes \cdots \otimes |1_1\rangle \otimes |1_0\rangle. \end{aligned}$$

Under this encoding, the truncated annihilation and creation operators are dense matrices in the computational basis. Correspondingly, $a^{(N)}$, $a^{(N)\dagger}$ and $n^{(N)}$ take the form of equations (1)–(3), now with each outer product acting on the N_q qubits representing the binary digits of n:

$$|n_i\rangle\langle n_j| \mapsto \bigotimes_{k=0}^{N_q-1} |b_k(n_i)\rangle\langle b_k(n_j)|. \quad (19)$$

The non-diagonal $|0\rangle\langle 1|$ and $|1\rangle\langle 0|$ terms are given by the previous ladder operators decomposed via the relation (17), while the remaining diagonal terms $|0\rangle\langle 0|$ and $|1\rangle\langle 1|$ can be expressed in terms of the Pauli-Z operator as

$$|0\rangle\langle 0| = \frac{I+Z}{2}, \quad |1\rangle\langle 1| = \frac{I-Z}{2}. \quad (20)$$

Although this encoding is logarithmically efficient in the number of qubits, the resulting operator strings are generally non-local and have higher weight compared to the unary case.

C. Symmetry-Based Reduction

When the full Hamiltonian conserves a quantity (for example the total excitation number $\hat{N}_{\text{tot}}$), the physical dynamics remain confined to symmetry sectors whose dimensions are typically much smaller than the full truncated Hilbert space. Exploiting these symmetries yields compact encodings that reduce both qubit count and gate complexity.

Let S be a conserved operator with eigenvalues s. If the initial state lies in the sector $S = s_0$, it suffices to encode the sector subspace $\mathcal{H}_{s_0}$ of dimension d_{s_0}. One then implements a logical mapping

$$\mathcal{H}_{s_0} \cong \mathbb{C}^{d_{s_0}} \longrightarrow \left(\mathbb{C}^2\right)^{\otimes m_s},$$

with $m_s = \lceil \log_2 d_{s_0} \rceil$ qubits. The mapping should be constructed so that the action of the Hamiltonian restricted to the sector becomes sparse (or block-diagonal) in the chosen logical basis.

This approach can be formally understood as a projection-based effective Hamiltonian construction which partitions the full Hilbert space into an active space (where the relevant physics occur) and an external space. By identifying the symmetry sector $\mathcal{H}_{s_0}$ as the active space, the effective Hamiltonian is obtained simply by projecting the full operator onto this subspace:

$$H_{\text{eff}}^{(s_0)} = \hat{P}_{s_0} H \hat{P}_{s_0},$$

where $\hat{P}_{s_0}$ is the projector onto the manifold defined by eigenvalue s_0. The resulting Hamiltonian $H_{\text{eff}}^{(s_0)}$ completely describes the system's evolution provided the initial state has no support outside $\mathcal{H}_{s_0}$.

Hence, there is no need to introduce a bosonic cutoff which leads to a dynamical leakage error scaling with simulation time and coupling strength since:

$$\| e^{-itH} \hat{P}_{s_0} - e^{-itH_{\text{eff}}^{(s_0)}} \hat{P}_{s_0} \| = 0.$$

TABLE I: Comparison of bosonic encodings for a truncated dimension N. When applicable, d_s denotes the dimension of a symmetry sector.

Encoding	Qubits required	Locality	Pauli density
Unary	N	local	low
Binary	$\lceil \log_2 N \rceil$	nonlocal	high
Symmetry	$\lceil \log_2 d_s \rceil$	sparse	low-medium

This circumvents the polynomial growth of the required basis size usually dictated by error bounds in non-conserving systems, allowing for precise simulations with a minimal, fixed number of qubits determined solely by the dimensions of the initial symmetry sector.

A feature summary of each encoding scheme is presented in Table I.

IV. Hamiltonian Simulation

The problem of Hamiltonian Simulation is to, given a local Hamiltonian $H = \sum_{j=1}^{m} H_j$, a time $t > 0$ and error $\epsilon_H > 0$, find a unitary U_t approximating e^{-iHt} such that

$$\left\| U_t - e^{-iHt} \right\| \leq \epsilon_H, \tag{21}$$

where $\|.\|$ denotes operator norm. Note that this is another source of error in addition to the truncation error discussed in Section II.

As established previously, the application of unary or binary qubit encodings map the truncated bosonic operators (and consequently the full Hamiltonian) into operators acting on a register of N qubits. Since the set of tensor products of Pauli matrices forms a complete basis for the space of linear operators on N qubits, the encoded Hamiltonian can always be rigorously decomposed as a real linear combination of Pauli strings:

$$H = \sum_{j=1}^{M} a_j P_j, \tag{22}$$

where $a_j \in \mathbb{R}$ are the expansion coefficients and each P_j is a Pauli string of the form

$$P_j = \bigotimes_{k=1}^{N} \sigma_{c_j(k)}^{(k)}, \tag{23}$$

with $\sigma_{c_j(k)}^{(k)} \in \{I, X, Y, Z\}$ acting on the k-th qubit. The problem is thus reduced to implementing the unitary evolution generated by this sum of non-commuting terms on a quantum computer.

A. Trotterization (Product Formulas)

Since the terms P_j in Eq. (22) generally do not commute (i.e., $[P_j, P_k] \neq 0$), the exponential of the sum does not factorize into a simple product of exponentials. To simulate the evolution, we employ product formulas, commonly referred to as Trotterization, which approximate the continuous time evolution by a sequence of discrete, short-time steps.

The simplest such approximation, named the first-order Lie-Trotter formula, decomposes the evolution over a total time t into r discrete steps of duration $\delta t = t/r$:

$$U(t) = e^{-i\sum_{j=1}^{M} a_j P_j t} \approx \left(\prod_{j=1}^{M} e^{-i a_j P_j \delta t} \right)^r. \tag{24}$$

The error induced by this approximation is determined by the non-commutativity of the Hamiltonian terms. Specifically, the spectral-norm distance between the ideal and approximated unitaries is bounded by [10]:

$$\left\| e^{-iHt} - \left(\prod_{j=1}^{M} e^{-i a_j P_j t/r} \right)^r \right\| \leq \frac{t^2}{2r} \sum_{1 \leq j < k \leq M} \|[a_j P_j, a_k P_k]\| + \mathcal{O}\left(\frac{t^3}{r^2} \right). \tag{25}$$

This bound can be simplified by exploiting the algebraic properties of Pauli strings. Two Pauli strings P_j and P_k either commute or anticommute. If $[P_j, P_k] = 0$, the commutator vanishes. If they anticommute, $\{P_j, P_k\} = 0$, implying $[P_j, P_k] = 2P_jP_k$. Since Pauli strings are unitary and hermitian, $\|P_jP_k\| = 1$, leading to the simplified commutator norm $\|[a_jP_j, a_kP_k]\| = 2|a_ja_k|$. The error bound thus reduces to a sum over the anticommuting pairs $\mathcal{A} = \{(j,k) \mid j < k, \{P_j, P_k\} = 0\}$:

$$\left\| e^{-iHt} - \left(\prod_{j=1}^{M} e^{-i a_j P_j t/r} \right)^r \right\| \lesssim \frac{t^2}{r} \sum_{(j,k) \in \mathcal{A}} |a_j a_k|. \tag{26}$$

This indicates that the circuit depth r required to suppress the simulation error scales quadratically with time t and depends on the total weight of anticommuting terms in the encoded Hamiltonian.

To improve the convergence rate, higher-order product

formulas can be utilized. The second-order Suzuki-Trotter formula symmetrizes the ordering of the exponentials:

$$S_2(t) = \left(\prod_{j=1}^{M} e^{-ia_j P_j \frac{t}{2r}} \prod_{j=M}^{1} e^{-ia_j P_j \frac{t}{2r}} \right)^r. \quad (27)$$

This symmetric sequence eliminates the first-order error terms, resulting in a total approximation error that scales as $\mathcal{O}(t^3/r^2)$. While each step of the second-order formula requires $2M$ exponentials (twice that of the first-order formula), the superior scaling often necessitates significantly fewer Trotter steps r to achieve a target precision ϵ_H, particularly for long-time simulations.

The fundamental advantage of decomposing the evolution into Pauli strings is the simplicity of implementing the individual factors $e^{-ia_j P_j \tau}$. Since $P_j^2 = I$, the exponential corresponds to a rotation in the Hilbert space:

$$e^{-ia_j P_j \tau} = \cos(a_j \tau) I - i \sin(a_j \tau) P_j. \quad (28)$$

Such an operator corresponds to a rotation by angle $2a_j\tau$ about the axis defined by P_j.

This method can be realized efficiently on quantum hardware using a sequence of basis-change gates, exploiting the parity of the Pauli string. A detailed circuit construction pipeline is provided in Appendix A.

B. Asymptotically Optimal Methods

In the query complexity model, the efficiency of a quantum simulation algorithm is quantified by the number of queries made to the oracle describing the Hamiltonian. While product formulas are standard, their query cost scales polynomially with the inverse precision. For example, a $2k$-th order product formula typically requires a number of queries scaling as $\mathcal{O}(t^{1+1/2k}/\epsilon^{1/2k})$ to simulate evolution for time t with error ϵ.

To achieve optimal scaling, particularly logarithmic dependence on the inverse precision, one employs algorithms based on block encodings. Formally, a unitary U acting on m ancilla qubits and n system qubits is said to be an (α, m)-block encoding of a matrix H acting on n qubits if

$$(\langle 0|^{\otimes m} \otimes I) U (|0\rangle^{\otimes m} \otimes I) = \frac{H}{\alpha}. \quad (29)$$

Here, $\alpha \geq \|H\|$ is a normalization constant that ensures unitarity.

Techniques such as Linear Combination of Unitaries and Qubitization [11] utilize this framework to synthesize functions of the Hamiltonian. These methods have been unified under the framework of Quantum Signal Processing [12] and later Quantum Singular Value Transformations [13]. This approach allows for the implementation of polynomial approximations of functions of the eigenvalues of the encoded Hamiltonian. Naturally this can be applied to the Quantum Simulation problem [13]:

Theorem IV.1 (QSVT-based Hamiltonian Simulation)**.** *Given an (α, m)-block encoding of a Hamiltonian H, the time evolution operator e^{-iHt} can be implemented with error at most ϵ with a query complexity of*

$$\mathcal{O}\left(\alpha t + \frac{\log(1/\epsilon)}{\log\left(e + \frac{\log(1/\epsilon)}{\alpha t}\right)} \right). \quad (30)$$

V. Application to light-matter interaction models

The presented bosonic truncation and qubit encoding techniques can be directly applied to simulate light-matter interaction models, such as the Jaynes-Cummings model and its generalizations. In this section we apply the developed framework to the Hamiltonian simulation of these models, analyzing resource requirements, error bounds and extracting relevant physical behaviour.

A. Symmetry-based simulation of the Jaynes–Cummings model

The Jaynes-Cummings (JC) model is a paradigmatic description of light-matter interaction, characterizing a two-level atom interacting with a single quantized bosonic mode. The Hamiltonian is given by:

$$H_{JC} = \hbar\omega_c a^\dagger a + \hbar \frac{\omega_a}{2} \sigma_z + \hbar g (a^\dagger \sigma_- + a \sigma_+), \quad (31)$$

where ω_c and ω_a are the cavity and atomic frequencies, respectively, and g is the coupling strength. A crucial feature of this model is the conservation of the total excitation number, $\hat{N}_{tot} = a^\dagger a + \sigma_+ \sigma_-$, such that $[\hat{N}_{tot}, H_{JC}] = 0$. This symmetry ensures that the dynamics are confined to invariant subspaces (sectors) labeled by the integer eigenvalue n of $\hat{N}_{tot}$.

Leveraging the symmetry-based reduction scheme proposed in Sec. III C, we circumvent the need for a large truncation cutoff N by restricting the simulation to specific excitation sectors $\mathcal{H}_n$. For a given sector n, the effective Hamiltonian reduces to a 2×2 block acting on the basis $\{|n-1, e\rangle, |n, g\rangle\}$ (for $n \geq 1$).

Projecting the full Hamiltonian onto this basis yields the 2×2 effective Hamiltonian:

$$H_{\text{eff}}^{(n)} = \begin{pmatrix} (n-1)\hbar\omega_c + \hbar\frac{\omega_a}{2} & \hbar g\sqrt{n} \\ \hbar g\sqrt{n} & n\hbar\omega_c - \hbar\frac{\omega_a}{2} \end{pmatrix}. \quad (32)$$

To implement this on a quantum processor, we decompose $H_{\text{eff}}^{(n)}$ into a linear combination of Pauli operators acting on a single qubit (in units of $\hbar$):

$$H_{\text{eff}}^{(n)} = (n - \frac{1}{2})\omega_c I + g\sqrt{n} X + \frac{\Delta}{2} Z, \quad (33)$$

where $\Delta = \omega_a - \omega_c$ is the atom-cavity detuning. This decomposition provides an exact mapping to a single

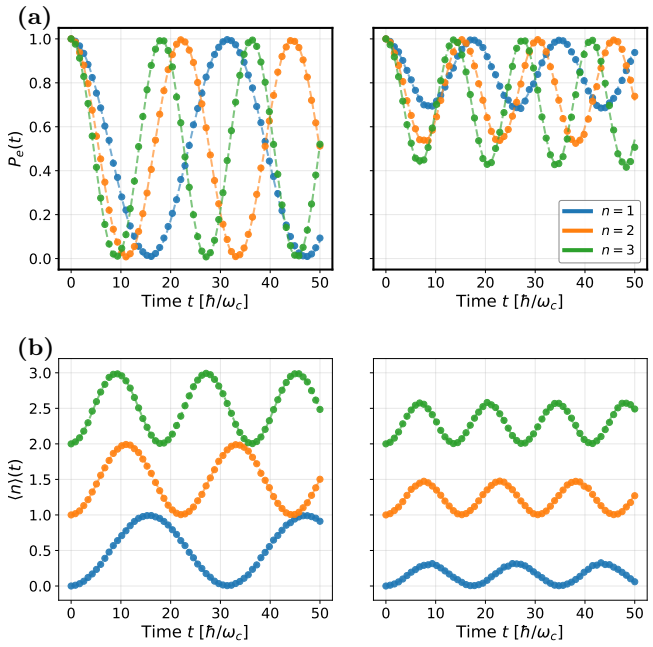

Fig. 1: Noisy Jaynes-Cummings dynamics. Time evolution of **(a)** excited-state population $P_e(t)$ and **(b)** mean photon number $\langle n \rangle(t)$ for excitation sectors $n = 1$ (blue), 2 (orange), and 3 (green). Columns compare the resonant ($\omega_a = \omega_c$, left) and detuned ($\omega_a = 1.3\omega_c$, right) regimes. Dashed lines indicate exact analytical solutions; dots indicate Trotter simulations (30 steps, 5000 shots) incorporating thermal relaxation noise.

qubit without leakage error, significantly reducing the resource overhead compared to unary or binary encodings. We demonstrate this approach by simulating the noisy dynamics of the JC model on a quantum processor. The evolution was implemented using a first-order Trotter expansion (Eq. 24) with 30 steps. To assess robustness, we incorporated thermal relaxation noise channels (T_1, T_2) characteristic of current hardware.

The results are presented in Fig. 1. In the resonant regime ($\omega_a = \omega_c$), we observe full-contrast Rabi oscillations. Crucially, the oscillation frequency scales with the sector index as $\Omega_n = 2g\sqrt{n}$, a signature of the quantization of the bosonic field. This $\sqrt{n}$ scaling is clearly visible as the $n = 3$ sector (green) oscillates significantly faster than the $n = 1$ sector (blue).

As expected for the JC interaction, the atom and cavity exchange energy periodically; when the atom is in the ground state, the photon number is maximized, verifying the conservation of $\hat{N}_{tot}$.

The effects of detuning are also clearly visible. Here, the energy mismatch prevents complete population transfer, resulting in reduced amplitude oscillations and a shift in the effective Rabi frequency to $\Omega'_n = \sqrt{4g^2 n + \Delta^2}$. Throughout the simulation, the Trotterized results show excellent agreement with the exact analytical solution (maximum error of the order $\sim 10^{-1}$) given the choice of parameters (See Appendix B), although thermal noise

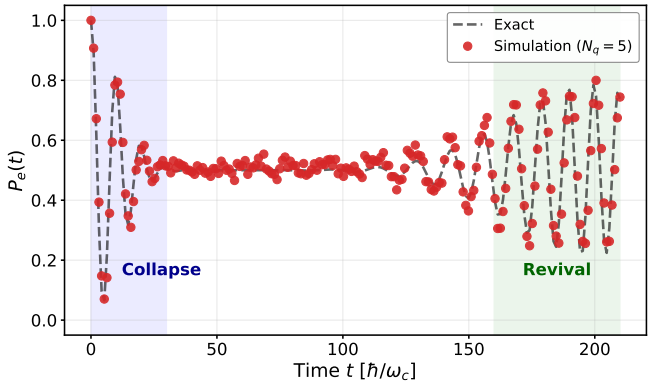

Fig. 2: Collapse and Revival of Rabi Oscillations. Time evolution of the atomic excited-state population $P_e(t)$ for an atom interacting with a quantized cavity field initialized in a coherent state ($\mu = 9$). The signal initially decays (*Collapse*, blue region) due to dephasing and later reconstructs (*Revival*, green region) around $t_R \approx 188\hbar/\omega_c$.

induces a very slight decay in signal amplitude over time, driving the system toward a mixed state. Note that there is no cutoff error here.

A more thorough exploration, including derivations and additional numerical results, is provided in Appendix B.

B. Dynamics of Coherent States on the Jaynes-Cummings Model

While the symmetry-based reduction is optimal for Fock states, general quantum simulation tasks often require preparing states that are superpositions of different excitation numbers, such as coherent states. Since these states do not belong to a single conserved symmetry sector, we must revert to a truncated bosonic basis and employ the rigorous error bounds established in Section II.

Let the initial bosonic state be the coherent state $|\alpha\rangle$ with mean photon number $\mu = |\alpha|^2$. The photon-number distribution is Poissonian,

$$\Pr(n) = e^{-\mu} \frac{\mu^n}{n!}, \tag{34}$$

and the tail weight above $N - 1$ is defined as:

$$p_{\text{tail}}(N) = \Pr(n \geq N) = 1 - \sum_{n=0}^{N-1} e^{-\mu} \frac{\mu^n}{n!}. \tag{35}$$

According to Theorem II.1 (tail-control guarantee), replacing the true initial state by its truncation onto $\mathcal{H}_N = \text{span}\{|0\rangle, \ldots, |N-1\rangle\}$ changes the expectation values of any unit-norm observable by at most $2p_{\text{tail}}(N)$. Consequently, to ensure the initial truncation error is bounded by $\varepsilon/2$, we must choose the smallest integer N satisfying

$$p_{\text{tail}}(N) \leq \varepsilon/2. \tag{36}$$

This can be done numerically or via standard bounds on the Poisson tail such as the Chernoff bound detailed

in Appendix C. For instance, in the limit where the mean photon number $\mu \gg 1$ and is much larger than the required precision ε, it is sufficient to take the cutoff

$$N \approx \mu\Big(1 + \sqrt{\frac{2}{\mu}\ln\frac{2}{\varepsilon}}\Big)$$

For our specific simulation, we targeted a mean photon number $\mu = 9$ (corresponding to a coherent amplitude $\alpha = 3$). After a numerical evaluation of the tail bound (Eq. 36) for a total precision tolerance $\varepsilon = 0.1$ we concluded that a cutoff of $N = 16$ would be sufficient. For context several truncation values are presented in Table II. This choice is particularly optimal for the Binary Encoding scheme discussed in Sec. III B, as the dimension $N = 16$ exactly fills a register of $N_q = \log_2(16) = 4$ qubits. Consequently, the full atom-cavity system is mapped to a dense Hilbert space of $N_q = 4 + 1 = 5$ qubits, maximizing resource efficiency without wasted subspace.

We simulated the resonant dynamics ($\omega_a = \omega_c$) of this system using the binary-encoded Hamiltonian constructed via Pauli decomposition. The results are displayed in Fig. 2. The dynamics of the atomic excited-state population $P_e(t)$ exhibit the signature *collapse and revival* phenomenon, a non-classical effect arising from the quantization of the electromagnetic field which is explained in detail in Appendix E.

Because the initial coherent state is a superposition of multiple Fock states $|n\rangle$, the time evolution is a sum of Rabi oscillations with incommensurate frequencies $\Omega_n = 2g\sqrt{n+1}$. At early times ($t \lesssim 30/\omega_c$), these frequency components dephase destructively, causing the high-contrast oscillations to dampen or "collapse" toward a quasi-steady value. However, unlike classical thermal decay, this dephasing is reversible. At the characteristic revival time $t_R \approx 2\pi\sqrt{\mu}/g$, the phases of the dominant photon number components re-synchronize, leading to a distinct resurgence in oscillation amplitude visible in the shaded region of Fig. 2.

While the chosen binary truncation $N = 16$ successfully captures the relevant interference effects of the photon distribution tail, there are slight deviations from the exact analytical solution, especially during later times. These discrepancies arise from a limited number of Trotter steps, which motivates seeking other better converging methods.

C. Dynamical Leakage and Vacuum Instability in the Rabi Model

While the Jaynes–Cummings model benefits from the conservation of total excitation number $\hat{N}_{tot}$, many physical regimes of light-matter interaction break this symmetry. A prominent example is the Quantum Rabi Model in the ultrastrong coupling (USC) regime, where the coupling strength g becomes comparable to the bare frequencies ω_c, ω_a. The Hamiltonian includes counter-rotating terms that were neglected in the RWA:

$$H_{\text{Rabi}} = H_{JC} + g(a^\dagger\sigma_+ + a\sigma_-). \tag{37}$$

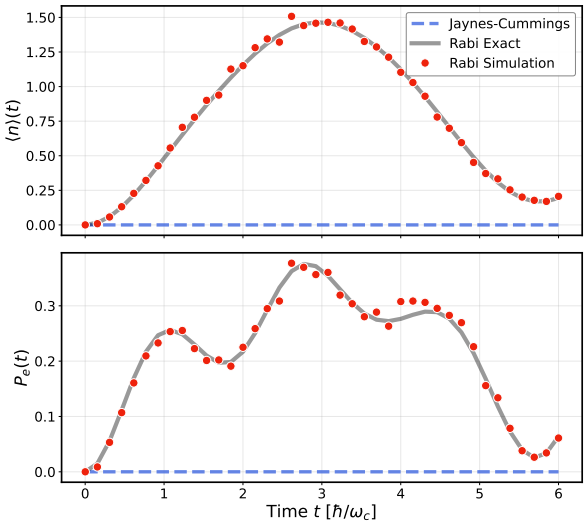

Fig. 3: Vacuum Instability in the Ultrastrong Coupling Regime. Comparison of the Jaynes–Cummings (JC) and Quantum Rabi models initialized in the ground state $|g, 0\rangle$. The simulation uses binary encoding with $N = 64$ (7 qubits) and $g/\omega_c = 0.8$.

These terms ($a^\dagger\sigma_+$ and $a\sigma_-$) allow for the simultaneous creation or annihilation of excitations in both the atom and the cavity, violating the conservation of $\hat{N}_{tot}$. Consequently, the dynamics are no longer confined to invariant subspaces, leading to *dynamical leakage* where the wavefunction spreads into higher photon number states over time.

To demonstrate this, we simulated the stability of the vacuum state $|\psi_0\rangle = |g, 0\rangle$. Under the JC Hamiltonian, this state is an eigenstate with zero energy, remaining invariant for all time. However, under the Rabi Hamiltonian, the counter-rotating terms couple $|g, 0\rangle$ directly to $|e, 1\rangle$, initiating a cascade of particle generation known as vacuum instability. Appendix G collects a series of results underpinning the Rabi-model phenomenology mentioned here including a time-dependent perturbative evaluation of the principal $|g, 0\rangle \to |e, 1\rangle$ channel and its characteristic frequency and analytical results which explain the complex beating and long-time structure of the dynamics.

These results mean that we must also account for dynamical leakage during the time evolution. To do so, and since the Jaynes-Cummings Hamiltonian satisfies equations (8)-(10), we invoke Theorem II.2.

Comparing the norm growth to the general constraint $\|H_w\Pi_{[0,\Lambda]}\| \leq \chi(\Lambda+1)^r$, we identify the scaling exponent $r = 1/2$ and the coupling parameter $\chi \approx 2g$. Then Theorem II.2 guarantees that there exists a truncation $\tilde{\Lambda}$ for which the evolution error on the initial subspace is also bounded by $\varepsilon/2$.

This informed the choice of using the binary encoding scheme with a cutoff $N = 64$ ($N_q = \log_2(N) + 1 = 7$ qubits) to simulate this regime with a coupling ratio $g/\omega_c = 0.8$. For a more explicit analysis see appendix F. The results, presented in Fig. 3, clearly illustrate the

distinctive behaviors. The JC dynamics remain frozen at zero population, verifying the symmetry protection. In contrast, the Rabi dynamics exhibit oscillations where the mean photon number $\langle a^\dagger a \rangle$ and excited population P_e rapidly increase from zero. This result explicitly validates the necessity of the dynamical leakage bounds provided by Theorem II.2 for non-conserving systems.

VI. Discussion and Conclusion

We have demonstrated the efficacy of finite-dimensional truncation schemes and qubit encodings for simulating bosonic light-matter interaction models. By exploiting the $U(1)$ symmetry of the Jaynes-Cummings (JC) model, we utilized a symmetry-based reduction to simulate exact Rabi dynamics in specific excitation sectors without leakage error. Furthermore, we employed binary encoding with rigorous tail-control bounds to successfully reproduce non-trivial macroscopic quantum phenomena, specifically the collapse and revival of Rabi oscillations in coherent states and the vacuum instability inherent to the Quantum Rabi model in the ultrastrong coupling regime.

Despite these successes, the fidelity of the simulations is intrinsically limited, especially by the Hamiltonian simulation algorithm employed. This limitation is particularly evident in the high qubit number simulation of the dynamics of the Rabi model, where slight deviations from the exact analytical solution appear as the Trotter error accumulates. While higher-order product formulas could mitigate this scaling, they come at the cost of increased circuit depth and gate count - one of the main limiting factors for simulating more complex circuits.

To address these scalability issues, future work should look toward asymptotically optimal algorithms. Techniques such as QSVT, while harder to implement, offer exponential improvements in precision dependence, making them superior candidates for high-precision simulations of complex bosonic Hamiltonians over extended time scales.

Nevertheless, it is notable that even with first-order Trotterization and in the presence of thermal relaxation noise characteristic of current hardware, we were able to extract meaningful physical behavior such as the characteristic $\sqrt{n}$ scaling of the Rabi frequency, the distinct separation of collapse and revival timescales, and the correlated generation of excitations from the vacuum in the Rabi model. This robustness validates the utility of the presented truncation and encoding frameworks for near-term quantum simulation. Although the models analyzed here are classically tractable and thus not candidates for demonstrating quantum advantage, they serve as essential benchmarks for verifying the fidelity of bosonic operations on digital quantum hardware.

VII. Personal Reflection

I found the exploration of bosonic truncation strategies and qubit encoding schemes to be particularly rewarding. Navigating the trade-offs between Hilbert space cutoffs and resource efficiency provided deep insight into the subtleties of digital quantum simulation. However, I remain skeptical regarding near-term demonstration of quantum advantage on simulating bosonic systems, as they have been extensively studied classically. Nevertheless, I thoroughly enjoyed the technical challenge of translating these continuous-variable systems into discrete quantum gate sequences with their current very limiting aspects, especially restricted gate counts.

Code Availability

All code required to reproduce the results in this work, including extra results and unary encoding tools is publicly available at `https://github.com/dmrapk/Quantum-Simulation-of-the-Jaynes-Cummings-Model`.

[1] J. H. Busnaina, Z. Shi, A. McDonald, D. Dubyna, I. Nsanzineza, J. S. C. Hung, C. W. S. Chang, A. A. Clerk, and C. M. Wilson, Nature Communications **15**, 3065 (2024).

[2] M. Tudorovskaya and D. Muñoz Ramo, Physical Review A **109**, 10.1103/physreva.109.032612 (2024).

[3] M. Hanada, J. Liu, E. Rinaldi, and M. Tezuka, Machine Learning: Science and Technology **4**, 045021 (2023).

[4] M. P. Woods, M. Cramer, and M. B. Plenio, Physical Review Letters **115**, 130401 (2015), arXiv:1504.01531 [quant-ph].

[5] Y. Tong, V. V. Albert, J. R. McClean, J. Preskill, and Y. Su, Quantum **6**, 816 (2022), arXiv:2110.06942 [quant-ph].

[6] Y. Zhang, X. Zhang, J. Sun, H. Lin, Y. Huang, D. Lv, and X. Yuan, WIREs Computational Molecular Science **15**, 10.1002/wcms.70020 (2025).

[7] S. Bravyi, D. P. DiVincenzo, and D. Loss, Annals of Physics **326**, 2793 (2011).

[8] M. Hanada, J. Liu, E. Rinaldi, and M. Tezuka, arXiv preprint (2022), arXiv:2212.08546 [quant-ph].

[9] B. Peng, Y. Su, D. Claudino, K. Kowalski, G. Hao Low, and M. Roetteler, Quantum Science and Technology **10**, 023002 (2025).

[10] A. M. Childs, Y. Su, M. C. Tran, N. Wiebe, and S. Zhu, Physical Review X **11**, 10.1103/physrevx.11.011020 (2021).

[11] G. H. Low and I. L. Chuang, Quantum **3**, 163 (2019).

[12] G. H. Low and I. L. Chuang, Physical Review Letters **118**, 10.1103/PhysRevLett.118.010501 (2017).

[13] A. Gilyén, Y. Su, G. H. Low, and N. Wiebe, in *Proceedings of the 51st Annual ACM SIGACT Symposium on Theory of Computing* (ACM, 2019) p. 193–204.

[14] J. R. Schrieffer and P. A. Wolff, Physical Review **149**, 491 (1966).

[15] D. Braak, Physical Review Letters **107**, 100401 (2011), arXiv:1103.2461 [cond-mat.stat-mech].

A. Parity-based implementation of Pauli-string exponentials

Simulating the evolution of a quantum system under a Hamiltonian $H = \sum_j a_j P_j$ via product formulas (e.g., Trotter-Suzuki) requires the implementation of unitary operators of the form $e^{-i\theta P}$, where $P = \bigotimes_{k=1}^{n} \sigma_k$ is an n-qubit Pauli string and $\theta = a_j \tau$ is a rotation angle.
Since standard quantum hardware typically implements native single-qubit rotations and two-qubit entangling gates (CNOTs), we must decompose these multi-qubit exponentials into these primitives. The general strategy relies on the fact that any Pauli string is unitarily equivalent to a string of Z operators (via local basis changes) and that a string of Z operators is related to a single-qubit Z rotation via parity computation.

1. Basis Changes and Operator Conjugation

We first establish the necessary identities for operator conjugation, starting with the mapping of local Pauli operators to the computational basis (Z).

Lemma A.1 (Single-qubit basis change)**.** *For any single-qubit Pauli operator $\sigma \in \{X, Y, Z\}$, there exists a Clifford unitary B such that $B\sigma B^\dagger = Z$. Specifically:*

$$HXH = Z, \tag{A1}$$

$$(HS^\dagger)Y(HS^\dagger)^\dagger = Z, \tag{A2}$$

$$IZI = Z. \tag{A3}$$

Proof. Direct matrix multiplication verifies these identities. For example,

$$S^\dagger Y S = \begin{pmatrix} 1 & 0 \\ 0 & -i \end{pmatrix} \begin{pmatrix} 0 & -i \\ i & 0 \end{pmatrix} \begin{pmatrix} 1 & 0 \\ 0 & i \end{pmatrix} = \begin{pmatrix} 0 & 1 \\ 1 & 0 \end{pmatrix} = X$$

and $HXH = Z$ thus $B = HS^\dagger$ maps $Y \to Z$. □

With local operators mapped to Z, we require a mechanism to compute the parity of the bitstring into a phase. This relies on the interaction between CNOT and Z.
Let $|x_1 \dots x_n\rangle$ denote a computational-basis state with bits $x_k \in \{0, 1\}$. The *bit-parity* is defined as

$$\text{parity}(x) = x_1 \oplus x_2 \oplus \cdots \oplus x_n,$$

which corresponds to the XOR of the constituent bits (0 for even number of ones, 1 for odd). The n-qubit operator $Z_1 Z_2 \cdots Z_n$ acts on these basis states by

$$\begin{aligned}(Z_1 \cdots Z_n)\,|x_1 \dots x_n\rangle &= (-1)^{x_1 + \cdots + x_n}\,|x_1 \dots x_n\rangle \\ &= (-1)^{\text{parity}(x)}|x_1 \dots x_n\rangle,\end{aligned}$$

so the product of Z operators encodes parity as a phase ($+1$ for even parity, -1 for odd parity).

Lemma A.2 (CNOT–Z conjugation)**.** *Let* CNOT$(c \to t)$ *denote the controlled-NOT gate. Then:*

$$\text{CNOT}(c \to t)\; Z_t\; \text{CNOT}(c \to t)^\dagger \;=\; Z_c Z_t. \tag{A4}$$

Proof. Evaluate the action on a computational basis state $|x_c x_t\rangle$. The CNOT maps this to $|x_c, x_t \oplus x_c\rangle$. Applying Z_t introduces a phase $(-1)^{x_t \oplus x_c}$. Undoing the CNOT returns the state to $|x_c x_t\rangle$ but retains the global phase. Since $(-1)^{x_t \oplus x_c} = (-1)^{x_t}(-1)^{x_c}$, the total action is identical to $Z_c Z_t$. □

2. Parity Compute and General Construction

We define the "parity compute" unitary, U_{parity}, as the operator that collects the parity information of a set of qubits into a chosen target qubit q_t.

Proposition A.3 (Parity compute identity)**.** *Let U_{parity} be the unitary implemented by a sequence (ladder) of* CNOT$(k \to q_t)$ *gates for all involved qubits $k \neq q_t$. Then:*

$$U_{\text{parity}}\; Z_{q_t}\; U_{\text{parity}}^\dagger \;=\; \bigotimes_{k=1}^{n} Z_k. \tag{A5}$$

Proof. We apply the identity from Eq. (A4) iteratively. Let the system comprise n qubits. We conjugate the central operator Z_{q_t} by one CNOT at a time.

$$\text{CNOT}(1 \to q_t) \dots \text{CNOT}(n \to q_t)\, Z_{q_t}\, \dots \text{CNOT}(1 \to q_t)^\dagger$$

Each conjugation step $\text{CNOT}(k \to q_t) Z_{q_t} \text{CNOT}(k \to q_t)^\dagger$ generates a Z_k factor on the control qubit while preserving the Z_{q_t} on the target. Repeating this for all $k \neq q_t$ results in the product $\prod_{k=1}^{n} Z_k$. □

This allows us to state the main theorem for simulating arbitrary Pauli exponentials, often referred to as the "Pauli Gadget."

Theorem A.4 (General Pauli String Exponentiation)**.** *Let $P = \bigotimes_{k=1}^{n} \sigma_k$ be an arbitrary Pauli string. Let $B = \bigotimes_{k=1}^{n} B_k$ be the tensor product of local basis change unitaries satisfying $B_k \sigma_k B_k^\dagger = Z_k$ (from Lemma A.1). For any target qubit q_t in the support of P:*

$$e^{-i\theta P} \;=\; B^\dagger\, U_{\text{parity}}^\dagger\, e^{-i\theta Z_{q_t}}\, U_{\text{parity}}\, B. \tag{A6}$$

Proof. First, we utilize the functional calculus property of unitary conjugation, $U e^A U^\dagger = e^{UAU^\dagger}$. Substituting the result from the Parity Compute Proposition:

$$U_{\text{parity}}^\dagger\, e^{-i\theta Z_{q_t}}\, U_{\text{parity}} = \exp\left(-i\theta\, U_{\text{parity}}^\dagger Z_{q_t} U_{\text{parity}}\right).$$

Note that in the Proposition we established $UZU^\dagger = \prod Z$. By unitarity, $U^\dagger(\prod Z)U = Z$. Inverting the logic for the CNOT ladder (which is its own inverse structure in the standard ladder case, or simply noting the conjugation direction), we establish that the CNOTs map the single

Z_{q_t} to the global $Z^{\otimes n}$ when viewed in the Heisenberg picture. Thus:

$$U_{\text{parity}}^{\dagger}\, e^{-i\theta Z_{q_t}}\, U_{\text{parity}} = e^{-i\theta(Z_1\otimes\cdots\otimes Z_n)}.$$

Finally, applying the basis change B:

$$B^{\dagger}\left(e^{-i\theta\prod Z_k}\right)B = \exp\left(-i\theta\bigotimes_k B_k^{\dagger}Z_kB_k\right) = \exp\left(-i\theta\bigotimes_k \sigma_k\right) = e^{-i\theta P}.$$

□

3. Algorithm and Resource Costs

The constructive implementation of the theorem above is detailed in Algorithm 1.

Algorithm 1 PauliGadget$(P, a\tau, q_t)$

```
Input: Pauli string P = ⨂_{k=1}^n σ_k, real aτ, target index q_t
for each qubit k = 1, ..., n do
    if σ_k = X then
        apply H on qubit k;
    else if σ_k = Y then
        apply S† then H on qubit k;
    end if
end for
for each k ∈ {1, ..., n} \ {q_t} do
    apply CNOT(k → q_t);
end for
apply R_Z(2aτ) on qubit q_t;
for each k ∈ {1, ..., n} \ {q_t} do
    apply CNOT(k → q_t) in reverse order;
end for
for each qubit k = 1, ..., n do
    undo the basis change applied in the first loop;
end for
Output: constructed gate sequence implementing e^{-iaτP}.
```

Resource Analysis

Let w be the weight of Pauli string P (the number of non-identity terms). The exact costs for a linear connectivity (ladder) implementation are:

- **CNOT Count:** $2(w-1)$. (Compute and uncompute parity).
- **Single-qubit Rotations:** Exactly 1 (R_Z on target).
- **Clifford Basis Gates:** At most $2w$ (Basis change and inverse).
- **Depth:** $O(w)$ for a linear ladder. This can be reduced to $O(\log w)$ by replacing the linear CNOT ladder with a tree-based parity accumulation network.

B. Symmetry-based analysis for the Jaynes-Cummings model

This appendix provides the step-by-step derivations that underpin the results presented in Sec V A of the main text. These calculations justify the plots and discussion in that same section of the main manuscript.

As mentioned, since $[H_{\text{JC}}, \hat{N}_{\text{tot}}] = 0$, dynamics preserve the excitation number and we may restrict to the invariant subspace with eigenvalue $n \in \mathbb{Z}_{\geq 1}$. A convenient orthonormal basis of this sector is

$$\{\,|n-1,e\rangle,\ |n,g\rangle\,\},$$

where $|e\rangle$ ($|g\rangle$) denotes the excited (ground) state of the two-level atom. The projector onto the sector is

$$\Pi_n = |n-1,e\rangle\langle n-1,e| + |n,g\rangle\langle n,g|.$$

The projected (effective) Hamiltonian is then given by $H_{\text{eff}}^{(n)} = \Pi_n H_{\text{JC}}\Pi_n$. Evaluating matrix elements in the ordered basis $\{|n-1,e\rangle, |n,g\rangle\}$ gives

$$H_{\text{eff}}^{(n)} = \begin{pmatrix} (n-1)\omega_c + \dfrac{\omega_a}{2} & g\sqrt{n} \\ g\sqrt{n} & n\omega_c - \dfrac{\omega_a}{2} \end{pmatrix}. \tag{B1}$$

Where the off-diagonal matrix element follow from $\langle n-1|a^{\dagger}|n\rangle = \sqrt{n}$ and the atom lowering/raising action on $\{|e\rangle, |g\rangle\}$.

Introducing the detuning $\Delta = \omega_a - \omega_c$ and writing the trace part explicitly we can rewrite the diagonal elements as,

$$\operatorname{tr} H_{\text{eff}}^{(n)} = (2n-1)\omega_c \quad \Rightarrow \quad \frac{\operatorname{tr} H_{\text{eff}}^{(n)}}{2} = \left(n-\tfrac{1}{2}\right)\omega_c.$$

Subtracting this scalar part and using the standard Pauli matrices X, Z in the chosen basis, one obtains the decomposition

$$H_{\text{eff}}^{(n)} = \left(n-\tfrac{1}{2}\right)\omega_c\, I + g\sqrt{n}\, X + \frac{\Delta}{2}\, Z. \tag{B2}$$

We can trivially check that the traceless part agrees with the matrix in Eq. (B1).

Now define the vector

$$\mathbf{v} = \left(g\sqrt{n},\ 0,\ \tfrac{\Delta}{2}\right), \qquad \|\mathbf{v}\| = \sqrt{g^2 n + \frac{\Delta^2}{4}}.$$

The eigenvalues of $H_{\text{eff}}^{(n)}$ are therefore

$$E_{\pm} = \left(n-\tfrac{1}{2}\right)\omega_c \pm \|\mathbf{v}\| = \left(n-\tfrac{1}{2}\right)\omega_c \pm \sqrt{g^2 n + \frac{\Delta^2}{4}}. \tag{B3}$$

And the energy splitting is

$$\Delta E \equiv E_+ - E_- = 2\|\mathbf{v}\| = \sqrt{4g^2 n + \Delta^2},$$

which motivates the definition of the generalized Rabi frequency

$$\Omega'_n \coloneqq \sqrt{4g^2 n + \Delta^2}. \tag{B4}$$

In the resonant case ($\Delta = 0$) this reduces to the familiar $\Omega_n = 2g\sqrt{n}$.
Since $H_{\text{eff}}^{(n)} = AI + \mathbf{v}\cdot\boldsymbol{\sigma}$ with $A = (n-\frac{1}{2})\omega_c$, the propagator restricted to the sector (setting $\hbar = 1$) is

$$\begin{aligned} U^{(n)}(t) &= e^{-iH_{\text{eff}}^{(n)}t} \\ &= e^{-iAt}\Big[\cos(\|\mathbf{v}\|t)\, I - i\sin(\|\mathbf{v}\|t)\,\frac{\mathbf{v}\cdot\boldsymbol{\sigma}}{\|\mathbf{v}\|}\Big]. \end{aligned} \tag{B5}$$

We will consider the initial state $|\psi(0)\rangle = |n-1, e\rangle$ (equivalently, the column vector $(1,0)^{\mathsf{T}}$ in the sector basis). The excited-state population at time t is

$$\begin{aligned} P_e(t) &= \big|\langle n-1, e|U^{(n)}(t)|n-1, e\rangle\big|^2 \\ &= \Big|\cos(\|\mathbf{v}\|t) - i\sin(\|\mathbf{v}\|t)\,\frac{v_z}{\|\mathbf{v}\|}\Big|^2 \\ &= \cos^2(\|\mathbf{v}\|t) + \frac{v_z^2}{\|\mathbf{v}\|^2}\sin^2(\|\mathbf{v}\|t) \\ &= 1 - \frac{v_x^2}{\|\mathbf{v}\|^2}\sin^2(\|\mathbf{v}\|t). \end{aligned} \tag{B6}$$

Substituting $v_x = g\sqrt{n}$ and $v_z = \Delta/2$, and using $\|\mathbf{v}\| = \frac{1}{2}\Omega'_n$, we obtain the convenient form

$$P_e(t) \;=\; 1 - \frac{4g^2 n}{4g^2 n + \Delta^2}\,\sin^2\Big(\tfrac{1}{2}\Omega'_n t\Big). \tag{B7}$$

On resonance ($\Delta = 0$) this reduces to

$$P_e(t) = \cos^2\big(g\sqrt{n}\,t\big) = 1 - \sin^2\big(g\sqrt{n}\,t\big), \tag{B8}$$

i.e. full-contrast Rabi oscillations at frequency $\Omega_n = 2g\sqrt{n}$.
In the two-level subspace the photon-number operator acts diagonally as

$$\hat{n}\big|_{\text{sector}} = \begin{pmatrix} n-1 & 0 \\ 0 & n \end{pmatrix}.$$

Therefore the expectation value is simply

$$\langle\hat{n}\rangle(t) = (n-1)P_e(t) + n\big(1 - P_e(t)\big) = n - P_e(t). \tag{B9}$$

Combining with Eq. (B7) gives the closed form

$$\langle\hat{n}\rangle(t) = n - 1 + \frac{4g^2 n}{4g^2 n + \Delta^2}\,\sin^2\Big(\tfrac{1}{2}\Omega'_n t\Big). \tag{B10}$$

Which on resonance reduces to $\langle\hat{n}\rangle(t) = n - \cos^2(g\sqrt{n}\,t) = n - \cos^2(\frac{1}{2}\Omega_n t)$, which oscillates between n and $n-1$ as energy is exchanged between atom and field.

a. Trotter error estimate used in numerical simulation In Sec. IV we stated the first-order Trotter error bound for a Hamiltonian decomposed as $H = \sum_j a_j P_j$ (see Eq. (26) of the main text). Specialising that result to the two nontrivial Pauli terms in Eq. (B2) (label them $a_1 P_1 = g\sqrt{n}\,X$ and $a_2 P_2 = \frac{\Delta}{2}\,Z$), these two Pauli matrices anticommute, hence the leading Trotter error per total time t with r steps behaves as

$$\begin{aligned} \Big\|e^{-iH_{\text{eff}}^{(n)}t} - \Big(e^{-ia_1P_1t/r}e^{-ia_2P_2t/r}\Big)^r\Big\| \;&\lesssim\; \frac{t^2}{r}\,|a_1 a_2| \\ &=\; \frac{t^2}{r}\,g\sqrt{n}\,\frac{|\Delta|}{2}. \end{aligned} \tag{B11}$$

We conclude that for fixed t and n, the Trotter error scales linearly with both the coupling strength g and the detuning $|\Delta|$. Note that on resonance ($\Delta = 0$) the Trotter error vanishes identically since the Hamiltonian terms commute. On the detuned case, a precision of $\epsilon_H \sim 0.1$ was chosen, informing our choice of parameters in the numerical simulations (while also maintaining RWA validity).

C. Tail bounds for coherent-state truncation

Let $X \sim \text{Poisson}(\mu)$. For any $t > 0$, Markov's inequality applied to e^{tX} yields

$$\begin{aligned} \Pr(X \ge k) \;&=\; \Pr\big(e^{tX} \ge e^{tk}\big) \;\le\; e^{-tk}\,\mathbb{E}\big[e^{tX}\big] \\ &=\; \exp\big(\mu(e^t - 1) - tk\big), \end{aligned} \tag{C1}$$

with stationary point

$$\mu e^{t^\star} = k \qquad\Longrightarrow\qquad t^\star = \ln\Big(\frac{k}{\mu}\Big), \tag{C2}$$

valid for $k > \mu$. Substituting $t^\star$ into (C1) yields the exact exponential bound

$$\begin{aligned} \Pr(X \ge k) &\le \exp\Big(\mu\Big(\frac{k}{\mu} - 1\Big) - k\ln\frac{k}{\mu}\Big) \\ &= \exp\Big(-\mu\Big[\frac{k}{\mu}\ln\Big(\frac{k}{\mu}\Big) - \frac{k}{\mu} + 1\Big]\Big). \end{aligned} \tag{C3}$$

Writing $k = (1+\delta)\mu$ with $\delta > 0$ yields the commonly used form

$$\Pr\big(X \ge (1+\delta)\mu\big) \le \exp\Big(-\mu\big[(1+\delta)\ln(1+\delta) - \delta\big]\Big). \tag{C4}$$

To ensure $p_{\text{tail}}(N) \le \varepsilon/2$ it suffices to choose $N = \lceil(1+\delta)\mu\rceil$ where $\delta > 0$ solves

$$\exp\Big(-\mu\big[(1+\delta)\ln(1+\delta) - \delta\big]\Big) \le \frac{\varepsilon}{2}. \tag{C5}$$

Equation (C5) is exact (within the Chernoff upper bound) but is implicit in δ and therefore typically inverted numerically.

For practical usage one often adopts the (simpler) multiplicative Chernoff inequality

$$\Pr\big(X \geq (1+\delta)\mu\big) \leq \exp\Big(-\frac{\mu\delta^2}{2+\delta}\Big), \qquad (\delta \geq 0), \quad \text{(C6)}$$

which follows from comparing the exponent in (C4) to the elementary lower bound

$$(1+\delta)\ln(1+\delta) - \delta \;\geq\; \frac{\delta^2}{2+\delta}, \qquad \delta \geq 0.$$

Using (C6) and imposing the tolerance $\varepsilon/2$ we obtain the sufficient condition

$$\exp\Big(-\frac{\mu\delta^2}{2+\delta}\Big) \leq \frac{\varepsilon}{2}. \quad \text{(C7)}$$

Defining the positive constant

$$c \;:=\; \frac{1}{\mu}\ln\Big(\frac{2}{\varepsilon}\Big) \;>\; 0, \quad \text{(C8)}$$

taking logarithms of (C7) and rearranging gives the algebraic inequality

$$\frac{\delta^2}{2+\delta} \;\geq\; c \quad\Longleftrightarrow\quad \delta^2 - c\,\delta - 2c \;\geq\; 0. \quad \text{(C9)}$$

Solving the quadratic equation $\delta^2 - c\delta - 2c = 0$ for δ and taking the positive root yields the closed-form choice

$$\begin{aligned}\delta \;&=\; \frac{c+\sqrt{c^2+8c}}{2} \\ &=\; \frac{1}{2\mu}\ln\Big(\frac{2}{\varepsilon}\Big) \;+\; \frac{1}{2}\sqrt{\Big(\frac{1}{\mu}\ln\Big(\frac{2}{\varepsilon}\Big)\Big)^2 + \frac{8}{\mu}\ln\Big(\frac{2}{\varepsilon}\Big)}\end{aligned} \quad \text{(C10)}$$

and therefore the (conservative) truncation dimension

$$N \;=\; \Big\lceil (1+\delta)\mu \Big\rceil \qquad \text{with } \delta \text{ given by (C10).} \quad \text{(C11)}$$

By construction (C11) guarantees $p_{\text{tail}}(N) \leq \varepsilon/2$ via the multiplicative Chernoff inequality (C6).

If $\ln(2/\varepsilon) \ll \mu$ (typical when μ is large and ε modest) then $c \ll 1$ and we can approximate

$$\delta \approx \sqrt{2c} = \sqrt{\frac{2}{\mu}\ln\Big(\frac{2}{\varepsilon}\Big)}, \qquad N \approx \mu\Big(1 + \sqrt{\frac{2}{\mu}\ln\frac{2}{\varepsilon}}\,\Big).$$

This recovers the familiar Gaussian scaling where the required excess above the mean scales like $O(\sqrt{\mu\ln(1/\varepsilon)}/\mu) = O\big(\sqrt{\ln(1/\varepsilon)/\mu}\big)$.

If $\ln(2/\varepsilon) \gg \mu$ then $c \gg 1$ and $\delta \approx c$, so $N \approx \mu(1+c) \approx \mu + \ln(2/\varepsilon)$. In this regime the closed-form bound correctly reflects that extremely small tolerances require adding approximately $\ln(1/\varepsilon)$ photons to the cutoff.

D. Practical cutoff choices for coherent initial states

Here we provide worked numerical recommendations for the bosonic truncation dimension when the initial bosonic state is a coherent state $|\alpha\rangle$ with mean photon number $\mu = |\alpha|^2$, see Table II. The initial-tail criterion is enforced by choosing the smallest integer N such that the Poisson tail $p_{\text{tail}}(N) = \Pr(n \geq N) \leq \varepsilon/2$. For dynamical leakage control we specialise Theorem II.2 to the common Jaynes–Cummings-type scaling $\|H_w \Pi_{[0,\Lambda]}\| \lesssim g\sqrt{\Lambda+1}$ (hence $r = \frac{1}{2}$, $\chi \approx g$) and adopt the conservative practical rule

$$\sqrt{\tilde{\Lambda}} = \sqrt{\Lambda_0} + C\,g\,t\,\log\Big(\frac{\Lambda_0 g t}{\varepsilon/2}\Big), \qquad \Lambda_0 = N-1, \quad C = 1,$$

then take $N_{\text{final}} = \max\{N, \tilde{\Lambda}\}$. If the simulated Hamiltonian strictly conserves total excitation and the initial state has been truncated to $\text{span}\{|0\rangle, \ldots, |N-1\rangle\}$, then evolution remains in that subspace and the dynamical containment parameter $\tilde{\Lambda}$ is not needed i.e. $N_{\text{final}} = N_{\text{exact/Chernoff}}$.

μ	ε	χt	N_{exact}	N_{Chernoff}	$p_{\text{tail}}(N_{\text{exact}})$	$\tilde{\Lambda}$	N_{final}
4	0.1	0.2	9	11	2.14×10^{-2}	13	13
4	0.1	1.0	9	11	2.14×10^{-2}	63	63
4	0.1	5.0	9	11	2.14×10^{-2}	1315	1315
4	0.01	0.2	11	14	3.02×10^{-3}	20	20
4	0.01	1.0	11	14	3.02×10^{-3}	116	116
4	0.01	5.0	11	14	3.02×10^{-3}	2423	2423
9	0.1	0.2	15	18	4.15×10^{-2}	21	21
9	0.1	1.0	15	18	4.15×10^{-2}	88	88
9	0.1	5.0	15	18	4.15×10^{-2}	1598	1598
9	0.01	0.2	19	22	2.43×10^{-3}	31	31
9	0.01	1.0	19	22	2.43×10^{-3}	155	155
9	0.01	5.0	19	22	2.43×10^{-3}	2834	2834
25	0.1	0.2	34	39	4.98×10^{-2}	46	46
25	0.1	1.0	34	39	4.98×10^{-2}	150	150
25	0.1	5.0	34	39	4.98×10^{-2}	2140	2140
25	0.01	0.2	40	45	3.44×10^{-3}	60	60
25	0.01	1.0	40	45	3.44×10^{-3}	232	232
25	0.01	5.0	40	45	3.44×10^{-3}	3493	3493

TABLE II: Calculated truncation choices for coherent states with mean photon number μ, target error ε, and interaction-strength-time product χt. N_{exact} is the minimal integer satisfying $p_{\text{tail}}(N) \leq \varepsilon/2$ (computed from the Poisson CDF). N_{Chernoff} is the closed-form conservative Chernoff bound. $\tilde{\Lambda}$ is the dynamical containment estimate specialised to $r = \frac{1}{2}$, and $C = 1$. The final working cutoff is $N_{\text{final}} = \max\{N_{\text{exact}}, \tilde{\Lambda}\}$.

E. Collapse and revival analysis

This appendix details the calculations that underpin the results concerning the collapse and revival of the atomic excited-state populations.

1. Exact expression for the atomic excited-state probability

Consider the Jaynes–Cummings Hamiltonian (on resonance)

$$H_{\rm JC} = \omega_c a^\dagger a + \frac{\omega_a}{2}\sigma_z + g\,(a^\dagger\sigma_- + a\sigma_+), \qquad \omega_a = \omega_c.$$

If the atom is initialized in the excited state $|e\rangle$ and the field in $|\alpha\rangle$, the initial state is

$$|\Psi(0)\rangle = |e\rangle \otimes |\alpha\rangle = \sum_{n=0}^{\infty} \sqrt{p_n}\,|e\rangle \otimes |n\rangle.$$

Because $H_{\rm JC}$ preserves total excitation number it decomposes into independent two-level dynamics between $|e,n\rangle$ and $|g,n+1\rangle$. The effective Rabi frequency associated with the n-th photon sector is then

$$\Omega_n \;=\; 2g\sqrt{n+1}.$$

Within that sector, if the atom is initially excited, the excited-state probability evolves as

$$P_e^{(n)}(t) \;=\; \cos^2\Big(\frac{\Omega_n t}{2}\Big) \;=\; \frac{1+\cos(\Omega_n t)}{2}.$$

Averaging over the initial Poisson weights gives the exact expression

$$P_e(t) \;=\; \sum_{n=0}^{\infty} p_n\,P_e^{(n)}(t) \;=\; \frac{1}{2}+\frac{1}{2}\sum_{n=0}^{\infty} p_n\cos\big(2gt\sqrt{n+1}\big). \tag{E1}$$

In practice the sum is truncated at $n \le N_{\rm exact}-1$ and the truncation error is bounded by $p_{\rm tail}(N_{\rm exact})$, chosen to be $\le \varepsilon/2$ above.

2. Asymptotic analysis: collapse envelope and revival times

To develop closed-form estimates for the collapse envelope and for the revival time, it is convenient to approximate the Poisson weights by a Gaussian near their peak when $\mu \gg 1$. Writing $n = \mu + x$ with $x = O(\sqrt{\mu})$, the Poisson distribution is approximated by

$$p_n \approx \frac{1}{\sqrt{2\pi\mu}} e^{-x^2/(2\mu)}.$$

Furthermore expanding the square root around μ:

$$\sqrt{n+1} = \sqrt{\mu+x+1} = \sqrt{\mu}\Big(1+\frac{x+1}{2\mu}-\frac{(x+1)^2}{8\mu^2}+\cdots\Big)$$

and retaining only the linear term in x (which controls dephasing at intermediate times) we obtain

$$2gt\sqrt{n+1} \approx 2gt\sqrt{\mu} \;+\; gt\frac{x+1}{\sqrt{\mu}}.$$

Substituting into the oscillatory sum in Eq. (E1) and approximating the sum by an integral over x gives (up to an overall phase)

$$\sum_n p_n e^{\,i2gt\sqrt{n+1}} \approx e^{\,i2gt\sqrt{\mu}}\,\exp\Big(-\tfrac{1}{2}g^2t^2\Big), \tag{E2}$$

i.e. the interference term acquires a Gaussian envelope with variance $\sigma^2 = (g^2)^{-1}$. Consequently the *collapse* of the initial high-contrast Rabi oscillations is characterized by the time-scale of the envelope,

$$t_{\rm env} \sim \frac{1}{g},$$

(we may take $t_{\rm collapse}$ as the time at which the envelope has decayed to a small fraction of its initial amplitude. Here $t \approx 1/g$ corresponds to the $1/e$ width). Note that this envelope estimate is a statement about the dephasing of many frequency components and is parametrically shorter than the revival time for large μ.

The *revival* mechanism is understood from the linearisation of $\sqrt{n+1}$ above. The key observation is that the phase difference between neighbouring n-components is approximately

$$\Delta\phi \approx 2gt\big(\sqrt{n+2}-\sqrt{n+1}\big) \approx \frac{gt}{\sqrt{\mu}}.$$

Rephasing (a revival) occurs whenever the relative phases accumulated across the dominant photon-number components differ by an integer multiple of 2π. Requiring $\Delta\phi \simeq 2\pi$ for adjacent components yields the standard revival time

$$t_R \;\approx\; \frac{2\pi\sqrt{\mu}}{g}. \tag{E3}$$

Because $t_R/t_{\rm env} \sim 2\pi\sqrt{\mu} \gg 1$ for $\mu \gg 1$, the initial collapse (rapid dephasing) and the later revival (rephasing) are well-separated in time. For the parameters used in Fig. 2 ($\mu = 9$) the leading-order revival time is $t_R \approx 2\pi\cdot 3/g = 6\pi/g$.

F. Bosonic truncation for Rabi model dynamics

This appendix presents a technical argument underpinning the bosonic truncation choice for the Rabi model dynamics starting from the vacuum state $|g,0\rangle$.

1. Short-time expansion of the mean photon number

Consider the Rabi Hamiltonian

$$H = \omega_c a^\dagger a + \tfrac{\omega_a}{2}\sigma_z + g\,\sigma_x(a+a^\dagger) \equiv H_0 + H_I.$$

In the Heisenberg picture we have,

$$n(t) = e^{iHt}\,n\,e^{-iHt} = n + it[H,n] + \frac{(it)^2}{2!}[H,[H,n]] + O(t^3).$$

Taking the expectation value in $|\psi_0\rangle$ and noting $\langle\psi_0|n|\psi_0\rangle = 0$ gives the leading nonzero term

$$\langle n(t)\rangle = \frac{t^2}{2}\,\langle\psi_0|[H,[H,n]]|\psi_0\rangle + O(t^3). \tag{F1}$$

The first commutator evaluates to

$$[H,n] = [g\,\sigma_x(a+a^\dagger),\, a^\dagger a] = g\,\sigma_x\,(a^\dagger - a).$$

And therefore the double commutator is

$$\begin{aligned}[H,[H,n]] &= [\omega_c a^\dagger a + \tfrac{\omega_a}{2}\sigma_z + g\sigma_x(a+a^\dagger),\; g\sigma_x(a^\dagger - a)] \\ &= g\big[\omega_c a^\dagger a,\; \sigma_x(a^\dagger - a)\big] + g\big[\tfrac{\omega_a}{2}\sigma_z,\; \sigma_x(a^\dagger - a)\big] \\ &\quad + g\big[g\sigma_x(a+a^\dagger),\; \sigma_x(a^\dagger - a)\big].\end{aligned}$$

Taking the expectation value in $|g,0\rangle$ leads to a cancellation of all terms that contain single Pauli matrix expectations (which vanish in the atomic ground state), leaving only the scalar term from the last commutator:

$$\langle\psi_0|[H,[H,n]]|\psi_0\rangle = 2g^2.$$

Therefore the short-time expansion reduces to

$$\langle n(t)\rangle = g^2t^2 + O(t^3). \tag{F2}$$

A straightforward way to turn the short-time growth into a truncation rule is to use Markov's inequality. For integer $N \geq 1$, this means

$$\Pr\{n \geq N\} \;=\; \Pr\{n/N \geq 1\} \;\leq\; \frac{\mathbb{E}[n]}{N} \;=\; \frac{\langle n(t)\rangle}{N}.$$

Demanding $\Pr\{n \geq N\} \leq \delta$ (tail tolerance δ) yields the sufficient criterion

$$N \;\geq\; \frac{\langle n(t)\rangle}{\delta}.$$

Combining with (F2) gives the short-time operational rule

$$N \;\gtrsim\; \frac{g^2t^2}{\delta} \quad \text{(short-time)}. \tag{F3}$$

This bound is conservative but explicit and more importantly provides a guide for the early-time burst of photons from the vacuum. It also explains the numerical observation in Sec. V C: for $g = 0.8$, $t \lesssim 1$ and $\delta = 10^{-2}$, $g^2t^2/\delta \approx 64$, so $N = 64$ is a justified choice to capture the initial dynamics.

2. Norm-growth identification and the specialised dynamical containment bound

Theorem II.2 guarantees that, for Hamiltonians satisfying the bandwidth and norm-growth constraints, there exists a dynamical truncation $\tilde{\Lambda}$ such that evolution from $[0,\Lambda_0]$ remains in $[0,\tilde{\Lambda}]$ to within prescribed tolerance. Specialising the theorem requires identifying the norm-growth exponent r and the prefactor χ for the Rabi Hamiltonian.

On the truncated block $\Pi_{[0,\Lambda]}$ the ladder operators obey

$$\|a\,\Pi_{[0,\Lambda]}\| = \sqrt{\Lambda}, \qquad \|a^\dagger\,\Pi_{[0,\Lambda]}\| = \sqrt{\Lambda+1},$$

and therefore

$$\|(a+a^\dagger)\Pi_{[0,\Lambda]}\| \leq \sqrt{\Lambda} + \sqrt{\Lambda+1} \leq 2\sqrt{\Lambda+1}.$$

Since the interaction term is $H_w = g\,\sigma_x(a+a^\dagger)$ and $\|\sigma_x\| = 1$, we obtain the bound

$$\|H_w\Pi_{[0,\Lambda]}\| \leq 2g\sqrt{\Lambda+1}.$$

This is of the form $\chi(\Lambda+1)^r$ with exponent $r = \frac{1}{2}$ and prefactor $\chi \approx 2g$. Inserting this identification into the practical formulation of Theorem II.2 yields the working dynamical containment estimate

$$\sqrt{\tilde{\Lambda}} \;=\; \sqrt{\Lambda_0} + C\,\chi\,t\,\log\Big(\frac{\Lambda_0\chi t}{\varepsilon_{\rm dyn}}\Big), \quad \text{with } \chi \approx 2g,\; r = \tfrac{1}{2}. \tag{F4}$$

If the initial state is the vacuum, evaluating (F4) with Λ_0 set conservatively to 1, yields a safe cutoff $\tilde{\Lambda}$.

We can then combine the short-time Markov rule (F3) with Eq. (F4) by considering:

$$N_{\rm final} \;=\; \max\Big\{\,\Big\lceil\frac{g^2t^2}{\delta}\Big\rceil,\;\; \lceil\tilde{\Lambda}\rceil + 1\Big\},$$

where δ is the acceptable tail probability for the observable of interest and $\tilde{\Lambda}$ is evaluated from (F4) with χ chosen as g or $2g$ depending on the conservative preference. In practice, since the final simulation time was in the "early-time" regime we can mainly consider the first argument, turning to $\tilde{\Lambda}$ only when a uniform, theorem-backed guarantee is required for long times.

G. An analysis on vacuum instabilty

In the discussed Rabi model, the dominant early-time channel that creates real photons is the transition $|g,0\rangle \to |e,1\rangle$ via the counter-rotating term of H_I. We will now work in the interaction picture with respect to H_0. The interaction-picture operator is

$$V_I(t) = g\big(\sigma_+(t) + \sigma_-(t)\big)\big(a(t) + a^\dagger(t)\big),$$

with $\sigma_+(t) = e^{i\omega_a t}\sigma_+$ and $a^\dagger(t) = e^{i\omega_c t}a^\dagger$. Then the amplitude (first-order Dyson term) to reach $|e,1\rangle$ is

$$c^{(1)}_{e,1}(t) = -i\int_0^t d\tau\;\langle e,1|\,V_I(\tau)\,|g,0\rangle = -ig\int_0^t e^{i(\omega_c+\omega_a)\tau}d\tau. \tag{G1}$$

Evaluating this integral yields

$$c^{(1)}_{e,1}(t) \;=\; g\,\frac{1 - e^{i(\omega_c+\omega_a)t}}{\omega_c+\omega_a}.$$

Hence the probability to occupy the one-photon sector via this channel is

$$\Pr(e,1;t) \;=\; \big|c^{(1)}_{e,1}(t)\big|^2 \;=\; \Big(\frac{2g}{\omega_c+\omega_a}\Big)^2 \sin^2\Big(\frac{(\omega_c+\omega_a)t}{2}\Big). \tag{G2}$$

For short times $(\omega_c+\omega_a)t \ll 1$ the small-angle limit recovers $\Pr(e,1;t) \approx g^2t^2$, consistent with the previous short-time result (F2). This further highlights that the dominant frequency of the counter-rotating-induced oscillation is $\omega_c+\omega_a$ (roughly 2ω on resonance), and that the amplitude scales as $(g/(\omega_c+\omega_a))^2$ for small g.

1. Schrieffer–Wolff (canonical) elimination and the Bloch–Siegert shift

A common analytic tool to capture dominant second-order effects of the counter-rotating terms (notably frequency shifts) is the canonical Schrieffer–Wolff [7, 14] unitary transformation that perturbatively eliminates those terms to leave an effective Hamiltonian with corrected energies. We begin by splitting the interaction into the energy-conserving (JC) and counter-rotating parts:

$$H_I = H_{\rm JC} + H_{\rm cr}$$

$$H_{\rm JC} = g(a^\dagger\sigma_- + a\sigma_+), \quad H_{\rm cr} = g(a^\dagger\sigma_+ + a\sigma_-).$$

The objective is to seek an anti-Hermitian generator S (with $S^\dagger = -S$) such that the unitary e^S approximately removes $H_{\rm cr}$ to leading order. The Baker–Campbell–Hausdorff expansion gives

$$H_{\rm eff} = e^S H e^{-S} = H + [S,H] + \tfrac{1}{2}[S,[S,H]] + \cdots .$$

So choosing S so that $H_{\rm cr} + [S,H_0] = 0$ eliminates $H_{\rm cr}$ at first order. A convenient ansatz for S is

$$S = \lambda\,(a^\dagger\sigma_+ - a\sigma_-)$$

with scalar λ to be determined. Computing the commutator with the free Hamiltonian $H_0 = \omega_c a^\dagger a + \frac{\omega_a}{2}\sigma_z$ gives:

$$[S,H_0] = \lambda\big([a^\dagger,\omega_c a^\dagger a]\sigma_+ + a^\dagger[\sigma_+,\tfrac{\omega_a}{2}\sigma_z] - \text{h.c.}\big).$$

Carrying out the algebra yields

$$[S,H_0] = -\lambda(\omega_c+\omega_a)\,(a^\dagger\sigma_+ + a\sigma_-).$$

Hence the condition $H_{\rm cr} + [S,H_0] = 0$ is satisfied by $\lambda = g/(\omega_c+\omega_a)$. With this choice the leading correction to the Hamiltonian arises at second order:

$$H_{\rm eff} \approx H_0 + H_{\rm JC} + \tfrac{1}{2}[S,H_{\rm cr}] + O(g^3).$$

Which evaluates to:

$$\tfrac{1}{2}[S,H_{\rm cr}] = \frac{g^2}{2(\omega_c+\omega_a)}[\,a^\dagger\sigma_+ - a\sigma_-,\, a^\dagger\sigma_+ + a\sigma_-\,].$$

By computing the commutator and simplifying one finds a diagonal effective correction proportional to σ_z:

$$\tfrac{1}{2}[S,H_{\rm cr}] \;=\; \frac{g^2}{\omega_c+\omega_a}\Big(\sigma_z\big(a^\dagger a + \tfrac{1}{2}\big)\Big).$$

Then projecting onto the low-photon sectors and collecting terms, the dominant effect is a shift of the two-level splitting (a "Bloch–Siegert-type" shift) and photon-dependent corrections. Thus the effective Hamiltonian to second order may be written schematically as

$$H_{\rm eff} \approx \omega_c a^\dagger a + \frac{1}{2}\big(\omega_a + \Delta_{\rm BS}\big)\sigma_z + g\,(a^\dagger\sigma_- + a\sigma_+) + \frac{g^2}{\omega_c+\omega_a}\,\sigma_z\,a^\dagger a + \cdots , \tag{G3}$$

with the leading Bloch–Siegert shift

$$\Delta_{\rm BS} \;=\; \frac{g^2}{\omega_c+\omega_a}, \tag{G4}$$

which is the conventional lowest-order result and is sufficient to explain spectral shifts observed in the USC regime. Higher-order terms generate photon-number dependent shifts (the $\sigma_z a^\dagger a$ term) and also induce higher-order dressing of eigenstates that are important for very large g/ω.

Alternatively, we can consider a non-perturbative approach. Although $H_{\rm Rabi}$ does not conserve excitation number, it does conserve a discrete $\mathbb{Z}_2$ parity:

$$\Pi = \sigma_z\, e^{i\pi a^\dagger a}, \qquad [H_{\rm Rabi},\Pi] = 0,$$

with eigenvalues ± 1. Diagonalisation is therefore block-diagonal in the two parity sectors.

This parity decomposition introduced by Braak [15] explains the appearance of near-degeneracies and avoided crossings in the USC spectrum, and the exact solution structure provides access to highly nonperturbative eigenstates that are used to benchmark numerical time evolution.